

Initial metal-metal bond breakage detected by fs X-ray scattering in the photolysis of Ru₃(CO)₁₂ in cyclohexane at 400 nm

Q. Y. Kong,^{a*} M. Laursen,^b K. Haldrup,^b K. S. Kjær,^b D. Khakhulin,^c E. Biasin,^{b,d} T. B. van Driel,^e M. Wulff,^f V. Kabanova,^f R. Vuilleumier,^{g,h} S. Bratos,ⁱ M. M. Nielsen,^b K. J. Gaffney,^d T. C. Weng,^{j*} M. H. J. Koch^k

Abstract Using femtosecond resolution X-ray solution scattering at a free electron laser we were able to directly observe metal-metal bond cleavage upon photolysis at 400 nm of Ru₃(CO)₁₂, a prototype for the photochemistry of transition metal carbonyls. This leads to the known single intermediate Ru₃(CO)₁₁(μ-CO)*, with a bridging ligand (μCO) and where the asterisk indicates an open Ru₃-ring. This loses a CO ligand on a picosecond time scale yielding the newly observed triple bridge intermediate, Ru₃(CO)₈(μ-CO)₃*. This loses another CO ligand to form the previously observed Ru₃(CO)₁₀, which returns to Ru₃(CO)₁₂ via the known single-bridge Ru₃(CO)₁₀(μ-CO). These results indicate that contrary to long standing hypotheses, metal-metal bond breakage is the only chemical reaction immediately following photolysis of Ru₃(CO)₁₂ at 400 nm. Combined with previous picosecond resolution X-ray scattering data and time resolved infrared spectroscopy these results yield a new mechanism for the photolysis of Ru₃(CO)₁₂.

^a Synchrotron Soleil, L'Orme des Merisiers St. Aubin, F- 91192 Gif-sur-Yvette, France.

^b Department of Physics, Technical University of Denmark, Fysikvej 307, DK-2800 Kongens Lyngby, Denmark.

^c European XFEL GmbH, Holzkoppel 4, D-22869 Schenefeld, Germany.

^d PULSE Institute, SLAC National Accelerator Laboratory, Menlo Park, California 94025, USA

^e LCLS, SLAC National Accelerator Laboratory, Menlo Park, California 94025, USA

^f European Synchrotron Radiation Facility, BP 220, F-38043 Grenoble Cedex, France.

^g Ecole Normale Supérieure, PSL Research University, UPMC Univ Paris 06, CNRS, Département de Chimie, PASTEUR, 24 rue Lhomond, F-75005 Paris, France.

^h Sorbonne Universités, UPMC Univ Paris 06, ENS, CNRS, PASTEUR, F-75005 Paris, France.

ⁱ Sorbonne Universités, UPMC Univ Paris 06, UMR 7600, LPTMC, F-75005 Paris, France.

^j Center for High Pressure Science & Technology Advanced Research, 1690 Cailun Rd, Bldg. 6-408, Pudong, Shanghai 201203, P.R.China.

^k European Molecular Biology Laboratory, Hamburg Outstation, EMBL c/o DESY, Notkestrasse 85, D-22603 Hamburg, Germany.

Introduction

Free electron lasers with intense ultrashort X-ray pulses of a few tens of femtoseconds (fs) offer unique opportunities to investigate the kinetics of the very early steps of photochemical reactions using pump-probe methods. These methods have recently been used in tracking excited-state electronic structural dynamics,¹ direct observation of bond formation,² atomistic characterization of solvation dynamics,³ visualization of non-equilibrium dynamics,⁴ and in favorable cases, observation of chemical bond dynamics of hot molecules^{5,6}, as well as conformational transitions in biological macromolecules.^{7,8} These experiments thus concentrated on physical rather than chemical processes. We used fs X-ray solution scattering to study the photolysis of Ru₃(CO)₁₂, a thermally stable metal carbonyl which serves as prototype for the photochemistry of transition metal carbonyls. Ru₃(CO)₁₂ is not only a useful catalyst, but also a precursor and building block in controlled photo-driven syntheses, whereby a specific chemical bond is broken at a specific wavelength.⁹⁻¹¹ The UV-visible spectrum of Ru₃(CO)₁₂ has two prominent absorption bands (Figure 1A). The first at 390 nm originates from a metal bonding to antibonding ($4d\sigma \rightarrow 4d\sigma^*$) transition which has long been hypothesized to result in heterolytic cleavage of a metal-metal (M-M) bond upon excitation. The second band at 238 nm is attributed to a metal to ligand charge transfer (MLCT) associated with the loss of a CO ligand.¹²⁻¹⁴

Due to its theoretical and practical interest, the cleavage of a M-M bond in the photolysis of Ru₃(CO)₁₂ has been extensively studied.¹⁵⁻¹⁹ The signals from ultrafast infrared (IR) spectroscopy following excitation of Ru₃(CO)₁₂ at 400 nm in non-coordinating solvents like C₆H₁₂ were interpreted as arising from two competing reactions, one involving metal-metal cleavage, the other resulting in loss of a CO ligand. These reactions were concluded to both yield intermediates with bridging CO ligands: Ru₃(CO)₁₁(μ-CO)* for the M-M cleavage channel and Ru₃(CO)₁₀(μ-CO) for the CO-loss channel (where the asterisk indicates a broken Ru-Ru bond).¹⁷ The CO-bridged intermediate Ru₃(CO)₁₁(μ-CO)* was first observed by time-resolved IR.²⁰ X-ray solution scattering with 100 ps resolution following 400 nm excitation of Ru₃(CO)₁₂ in C₆H₁₂ unambiguously confirmed the existence of Ru₃(CO)₁₀(μ-CO) but not Ru₃(CO)₁₁(μ-CO)* and revealed an additional major intermediate Ru₃(CO)₁₀ with terminal CO only.²¹ The existence of Ru₃(CO)₁₀ was independently confirmed by X-ray transient absorption spectroscopy with 100 ps resolution.²²

In previous ultrafast IR¹⁷ and 100 ps resolution X-ray scattering studies^{11,21} mixtures of CO loss and M-M bond breakage intermediates were observed. These measurements lacked the structural sensitivity or time resolution to

determine whether 400 nm excitation only leads to Ru-Ru bond dissociation with CO loss the product of a secondary process or if direct CO dissociation can be achieved with 400 nm excitation.

The origin of the major photoproduct at 100 ps, $\text{Ru}_3(\text{CO})_{10}$, also remained unclear. Successive single CO loss from $\text{Ru}_3(\text{CO})_{12}$ has been proposed,²³ because simultaneous loss of two CO from $\text{Ru}_3(\text{CO})_{12}$ in solution following single photon absorption at 400 nm is unlikely²³ and has not been experimentally proven.

In the present study we used the fs time resolution of the XPP end station²⁴ at the LCLS X-ray Free Electron Laser²⁵ to determine the species formed about 100 fs after photoexcitation. Figure 1 displays the X-ray solution scattering pattern of the Ru-Ru bond breakage intermediate $\text{Ru}_3(\text{CO})_8(\mu\text{-CO})_3^*$ after laser excitation of $\text{Ru}_3(\text{CO})_{12}$ at 400 nm. Details of the experimental procedures and data reduction are described in the materials and methods section. The conditions of the previous experiments are summarized and compared with present ones in Table S1 in the ESI.

Results

Our analysis relies on difference scattering patterns obtained by subtracting the pattern measured without laser excitation from all other ones in the time series, as described in the data reduction section. Selected difference patterns ($q\Delta S(q,t)$) illustrating the structural changes due to the laser excitation are shown in Figure 2A as a function of the momentum transfer $q = 4\pi\sin\theta/\lambda$, where 2θ is the scattering angle and λ the X-ray wavelength (1.305 Å).

The kinetics of the reaction is modelled by analysing the experimental difference scattering patterns at different times using linear combinations of the difference scattering patterns of the equilibrium structures of putative intermediates obtained by DFT calculations. Note that only the fraction of molecules which has not returned to the ground state in the first 100 fs contributes to the signal. This fraction was obtained by scaling the scattering data and the simulated Debye scattering of the intermediates and $\text{Ru}_3(\text{CO})_{12}$ to one solvent molecule. The simulated Debye scattering was divided by 4628, corresponding to the number of solvent molecules surrounding one $\text{Ru}_3(\text{CO})_{12}$ molecule at a concentration of 2mM. Linear combination fitting of the data at 100 fs gives a fraction of 0.26 (or 9.83×10^9 molecules in the irradiated volume) for $\text{Ru}_3(\text{CO})_{11}(\mu\text{-CO})^*$ and 0.74 for $\text{Ru}_3(\text{CO})_{12}$ in the ground state.

As the catalyst works in a cycle, the intermediates must remain close to equilibrium and one may assume that the time and spatially averaged structures of these intermediates, the only ones accessible by X-ray scattering, do not differ too much from those of the putative intermediates. The total scattering signal arises from three contributions, scattering from the solute, solvent and solute-solvent interaction (cage)^{11,21} as described in Figure 2B and Figures S2, S3 in the ESI. These model difference X-ray scattering intensities (Figures S2b and S2c) confirm that each species generates a distinct signal making ultrafast X-ray scattering a tool enabling to detect all transient structures including optically silent ones.^{11,21}

As in previous studies we considered an extensive set of potential reaction intermediates (Figure S1). Only $\text{Ru}_3(\text{CO})_{10}(\mu\text{-CO})$ and $\text{Ru}_3(\text{CO})_{10}$ were found indispensable to fit the experimental data at times above 50 ps. In order to obtain a good fit at time delays below 10 ps in the present study, it was necessary to include $\text{Ru}_3(\text{CO})_{11}(\mu\text{-CO})^*$, which had so far only been characterized by its IR signature,^{17,20} and additionally a new intermediate, the triple-bridge $\text{Ru}_3(\text{CO})_8(\mu\text{-CO})_3^*$ (Figure S2a) with a broken Ru-Ru bond. The other intermediate with similar structure $\text{Ru}_3(\text{CO})_9(\mu\text{-CO})_3^*$ (isomer2 in Figure S1) did not give a good fit. $\text{Ru}_3(\text{CO})_{11}$ with terminal CO only was initially assumed to be the precursor of $\text{Ru}_3(\text{CO})_{10}(\mu\text{-CO})$ ^{9,17} and included in the fit, but rejected as it did not improve the fit as illustrated in Figures 3B and 3C. Figure 3A displays a set of difference signals, $q\Delta S(q,t)$, representing key features at fs and ps time delays. As illustrated in Figure 2B, the strong negative feature at $q = 1.3 \text{ \AA}^{-1}$ and signals below this value arise mainly from solvent heating,²⁶ the positive shoulder at $1.4 < q < 1.8 \text{ \AA}^{-1}$ is a combination of solute and cage with a small contribution from the solvent, while signals at $q > 2 \text{ \AA}^{-1}$ arise mainly from changes in the solute structure. These signals display distinct features revealing that different transient structures are formed. In Figure 3A the significant positive feature at $q = 4 \text{ \AA}^{-1}$ at $t = 100 \text{ fs}$ is split at 5.16 ps, following which the difference signal evolves to a broad oscillation from $q = 2.3 \text{ \AA}^{-1}$ to $q = 4.5 \text{ \AA}^{-1}$ at 45 ps. Comparison of the experimental $q\Delta S(q,t)$ with those arising from different transient structures illustrate that $\text{Ru}_3(\text{CO})_{11}(\mu\text{-CO})^*$ (M-M broken, single bridge) is the only species at the onset of the reaction (Figure 3B), while the $q\Delta S(q,t)$ arising from $\text{Ru}_3(\text{CO})_8(\mu\text{-CO})_3^*$ best describes the data at $t = 5.16 \text{ ps}$ (Figure 3C). When all intermediates were included in the fit, only $\text{Ru}_3(\text{CO})_{11}(\mu\text{-CO})^*$ and $\text{Ru}_3(\text{CO})_8(\mu\text{-CO})_3^*$ remained at 100 fs and 5.16 ps respectively, while the contribution of other intermediates converged to zero within fitting uncertainties. The $q\Delta S(q,t)$ at $t = 45 \text{ ps}$ is fully consistent with our previous X-ray scattering data at 50 ps (Figure 3D), where $\text{Ru}_3(\text{CO})_{10}$ was determined to be the major photoproduct.²¹

To elucidate the kinetics a two-step approach of single-point and global analysis was applied (detailed in the ESI). The experimental $q\Delta S(q,t)$ at 170 different time delays were fitted (Figure 2A) to obtain the kinetics. The single-point procedure yields the concentration of each species at each time delay as shown by the individual markers in Figure 4. Deviations from the equilibrium structures of the intermediates due to vibrational excitations (“hot molecules”) mainly influence the data below 1-3 ps as illustrated in Figure S4 by the poorer fits at short times. Even though the results of this analysis have significant uncertainties, as evident from the scatter in Figure 4, they allow the identification of a potential kinetic model that can be applied within a global fitting analysis. In this second step of the analysis, the time evolution of each transient species is constrained to conform to a kinetic model allowing robust determination of the reaction constants. The global fitting is described in detail in the ESI and in Figure S5. The full lines in Figure 4 illustrate the time evolution of each species following this more quantitative analysis.

Laser radiation at 400 nm selectively excites the $4d\sigma \rightarrow 4d\sigma^*$ transition in Ru which triggers cleavage of one of the Ru-Ru bonds and subsequent redistribution of charge. As a result one of the equatorial CO ligands rebinds in the bridge location between another pair of Ru atoms forming the $\text{Ru}_3(\text{CO})_{11}(\mu\text{-CO})^*$ transient at the onset of the reaction. This loses one CO ligand to form the triple-bridge species $\text{Ru}_3(\text{CO})_8(\mu\text{-CO})_3^*$ at 1.5 ps with a reaction rate constant of $6.6 \pm 0.5 \times 10^{11} \text{ s}^{-1}$.

It is possible that this intermediate does not form at low radiant fluence. Another possibility is that it escaped detection in time-resolved IR studies.¹⁷ Indeed, according to DFT calculations the triple-bridge $\text{Ru}_3(\text{CO})_8(\mu\text{-CO})_3^*$ has three IR absorption bands originating from the stretching mode of bridging CO which either overlap with the absorption of $\text{Ru}_3(\text{CO})_{11}(\mu\text{-CO})^*$ or the terminal CO, as illustrated in Figure S6. If the intermediates are independent of the radiant fluence the present results and those of our previous 100 ps X-ray scattering studies^{11,21} would provide a good example illustrating the potential of ultrafast X-ray scattering in the detection of optically silent transient structures during a chemical reaction. $\text{Ru}_3(\text{CO})_8(\mu\text{-CO})_3^*$ transforms into $\text{Ru}_3(\text{CO})_{10}$ at 10 ps with a reaction rate constant of $1 \pm 0.2 \times 10^{11} \text{ s}^{-1}$ by loss of a second CO. $\text{Ru}_3(\text{CO})_{10}$ becomes the major transient structure after 10 ps.

A reduced kinetic model without the triple-bridge intermediate was evaluated against the full model involving the $\text{Ru}_3(\text{CO})_8(\mu\text{-CO})_3^*$ using a statistical F-test. We conclude with 99.7% confidence that the full kinetic model represents the experimental data better. The F-test evaluation is described in the ESI, and the result is shown in Figure S7. A direct comparison of the experimental difference X-ray scattering intensity $q\Delta S(q,t)$ at 5.16 ps with the reduced and the full model also confirms the formation of $\text{Ru}_3(\text{CO})_8(\mu\text{-CO})_3^*$ (Figure S8 in the ESI). The reduced model is also less likely because it implies the simultaneous loss of two CO in its first reaction step. The fact that the dominating intermediate $\text{Ru}_3(\text{CO})_{11}(\mu\text{-CO})^*$ is the same in the IR experiments done at low radiant fluence¹⁷ and in our experiments strongly suggests that significant multiphoton excitation can be ruled out.

Femtosecond X-ray solution scattering clearly demonstrates the selective Ru-Ru breakage in $\text{Ru}_3(\text{CO})_{12}$ excited at 400 nm and excludes any competing primary reactions. The origin of the major photoproduct $\text{Ru}_3(\text{CO})_{10}$ previously observed in 100 ps X-ray studies^{11,21,22} is also simply explained by the full model. It is formed through successive CO loss from $\text{Ru}_3(\text{CO})_{12}$ via two intermediates $\text{Ru}_3(\text{CO})_{11}(\mu\text{-CO})^*$ and $\text{Ru}_3(\text{CO})_8(\mu\text{-CO})_3^*$. The time course of the weights of the two solvent components is also obtained from the data fitting and shown in Figure S9. A detailed description of the solvent contribution is given in the ESI.

To gain direct information about the molecular structure of the reaction intermediates and infer the reaction mechanism, the solute-only difference signal was obtained by subtracting the contribution from bulk solvent response and changes in the solvation cage structure (by MD simulations) from the measured signals.¹¹

In Figure 5A the solute-only difference signals at three key time delays are compared with the difference signal of the intermediates determined to be dominating at those time delays and in each case good agreement between the model and the data is observed. Whereas in spectroscopy the signatures of particular intermediates correspond to specific energies, in solution scattering the structural information is spread over the entire q -range. A more intuitive picture of the structural rearrangements is therefore provided by the difference Radial Distribution Function (DRDF) $r\Delta R(r,t)$ i.e. the sine transform of $q\Delta S(q,t)$ (described in the ESI), which represents the atom-atom pair distribution function during the course of the reaction. A positive peak in the DRDF indicates the presence of a new characteristic correlation length in the molecule, while a negative peak indicates loss of such a correlation length, often representative of a broken chemical bond. The experimental and theoretical $r\Delta R(r,t)$ at 100 fs, 5.16 ps and 45 ps shown in Figure 5B provide structural information about $\text{Ru}_3(\text{CO})_{11}(\mu\text{-CO})^*$, $\text{Ru}_3(\text{CO})_8(\mu\text{-CO})_3^*$ and $\text{Ru}_3(\text{CO})_{10}$, which are the dominant solute species at these time delays. Strong positive peaks at 5.2 Å at 100 fs and 5.4 Å at 5.16 ps are observed, which disappear at 45 ps. These arise from the newly formed long Ru...Ru distances in $\text{Ru}_3(\text{CO})_{11}(\mu\text{-CO})^*$ and $\text{Ru}_3(\text{CO})_8(\mu\text{-CO})_3^*$. The negative peaks at 2.9 Å at 100 fs, 3.5 Å at 5.16 ps and 3.3 Å at 45 ps correspond to the broken Ru-Ru bond compared to the parent molecule.

Some caution is, however, necessary when interpreting DRDFs, as both a limited q -range and peak overlap may lead to shifts in peak positions (Figure S10). The different negative peaks in Figure 5B arise from differently

overlapped Ru-Ru distances in $\text{Ru}_3(\text{CO})_{11}(\mu\text{-CO})^*$, $\text{Ru}_3(\text{CO})_8(\mu\text{-CO})_3^*$ and $\text{Ru}_3(\text{CO})_{10}$ with that in the parent molecule. The positive peaks of the long Ru...Ru distance in $\text{Ru}_3(\text{CO})_{11}(\mu\text{-CO})^*$ and $\text{Ru}_3(\text{CO})_8(\mu\text{-CO})_3^*$ are also shifted by about 0.2 Å compared to the molecular structures used to simulate the curves. With this offset in mind, the structural changes of the Ru_3 cluster following photolysis can be clearly visualized from the DRDFs presented in Figure 5C, illustrating the appearance of the positive peak at 5.2 Å at the onset of the reaction, its gradual shift towards longer distances in the middle of the reaction and its final disappearance at the end, which correspond to the Ru_3 ring opening and closing in the course of the reaction. In our previous synchrotron study with higher q -space coverage, the DFT calculated structures of $\text{Ru}_3(\text{CO})_{12}$ and $\text{Ru}_3(\text{CO})_{10}$ were optimized by direct structural fitting and a scaling factor for the DFT prediction was determined (Table S2).²¹ Applying the same scaling factor to the DFT optimized structure of $\text{Ru}_3(\text{CO})_8(\mu\text{-CO})_3^*$ yields Ru-Ru distances of 2.73, 2.83, and 5.18 Å.

Discussion

Although our results have some similarities with those of IR spectroscopy¹⁷ they also differ significantly. With IR, the signal attributed to $\text{Ru}_3(\text{CO})_{11}(\mu\text{-CO})^*$ increases during the first 50 ps and then decreases between 50-250 ps whereas here it continuously decreases up to 10 ps. The signal for $\text{Ru}_3(\text{CO})_{10}(\mu\text{-CO})$ is not observed here during the first 45 ps whereas IR suggests that it decreases up to 30 ps and then increases.¹⁷ In our previous study at 390 nm²¹ it was necessary to include this intermediate to obtain a good fit, but this was not the case at 260 nm.¹¹ Combining the information from time-resolved IR results¹⁷ with that of our previous study from 50 ps to 300 ns,^{11,21} and the current one from 100 fs to 50 ps, we propose a complete mechanism for the photofragmentation of $\text{Ru}_3(\text{CO})_{12}$ in C_6H_{12} following 400 nm laser excitation at high radiant fluence in Figure 6. Excitation selectively breaks a single Ru-Ru bond to form $\text{Ru}_3(\text{CO})_{11}(\mu\text{-CO})^*$. No competitive CO loss reaction is detected. $\text{Ru}_3(\text{CO})_{11}(\mu\text{-CO})^*$ loses one CO forming $\text{Ru}_3(\text{CO})_8(\mu\text{-CO})_3^*$ with a characteristic timescale of 1.5 ps, which in turn loses another CO and also reconstitutes the Ru-Ru bond to yield $\text{Ru}_3(\text{CO})_{10}$ on a time scale of 10 ps. $\text{Ru}_3(\text{CO})_{10}$ dominates from 10 ps to 100 ns,^{11,21} and rebinds one CO to form $\text{Ru}_3(\text{CO})_{10}(\mu\text{-CO})$,^{11,17,21} which eventually relaxes to the starting molecule by binding another CO.

Materials and Methods

Experimental Procedures

Our experiments were conducted during three 12h shifts distributed over consecutive days. Fresh samples of $\text{Ru}_3(\text{CO})_{12}$ in C_6H_{12} with a concentration of 2 mM were prepared around every 6 hours in order to minimize possible sample degradation. In the pump-probe experimental setup the sample was continuously flowed through a 100 µm diameter capillary nozzle, after which it was collected and recycled. This procedure produces a free flowing circular liquid jet of 100 µm diameter with flow direction perpendicular to both the laser-pump and X-ray probe pulses. The flow speed of the jet was set to 1.5 ml/min yielding a flow velocity of 3 m/s ensuring that the sample is renewed between each laser-pump and X-ray probe event. The optical laser system at the XPP station of LCLS provided femtosecond pump pulses (~14 µJ) at 400 nm with a full width at half maximum (fwhm) of 30-40 fs. These optical pulses were focused to ~100-150 µm² on the liquid jet. This corresponds to a radiant fluence of 1.28-3.85 TWcm⁻², which is much higher than in previous experiments as indicated in Table S1 in the ESI. More accurate laser parameters are difficult to estimate with the complex experimental setup, but they represent an upper limit. To ensure that the experiment was performed in the linear laser fluence regime, a set of power titration experiments were performed. Briefly, the difference signal for a range of laser fluences was acquired and analyzed in terms of a linear combination of solute and solvent contributions to the signal. The ratio of these two contributions was monitored as a function of fluence and was found to deviate from linearity at higher fluences. No multiphoton excitation of the solvent could be detected at the radiant fluence used for the experiment. The weak solute signal could not be investigated in detail. The 14 µJ pulses represent a compromise to avoid multiphoton excitation while still obtaining a reasonable signal within the allocated duration of the experiment. X-ray probe pulses were focused down to a spot size of ~20 µm² using beryllium lenses and set to spatially overlap with the laser pulses on the liquid jet. The experiment was operated in beam-sharing mode with only the diamond (111) monochromatized part of the full LCLS beam going to the XPP instrument. The X-ray probe pulses (~40 fs fwhm) had ~5 × 10¹⁰ photons/pulse with energy centered at 9.5 keV (relative bandwidth < 10⁻⁴) and a repetition rate of 120 Hz. Due to the group velocity mismatch between the visible light and the X-rays in liquid C_6H_{12} , which displaces the temporal overlap of the pump and probe pulses, the actual time resolution with a 100 µm liquid jet is ~100 fs. To correct for the temporal jitter in relative arrival times of the pump and the probe pulses a dedicated timing tool²⁷ was used throughout the measurements.

Data reduction.

The X-ray scattering data was reduced following the methodology described in detail in previous work (SI of ref 3). The 2D X-ray patterns of laser-pumped/unpumped $\text{Ru}_3(\text{CO})_{12}$ in C_6H_{12} were recorded on the CSPAD detector developed at the LCLS.²⁸ For every seventh shot the scattering pattern of the solution was recorded without pump; from these scattering patterns the laser-off signals were constructed as described below. Each scattering pattern was corrected for solid angle, flat field and X-ray polarization. In addition, the output of the detector was corrected to reduce common mode fluctuations. A mask was then applied to the corrected 2D patterns to remove bad pixels and shadowed regions of the detector. Subsequently, the 2D images were azimuthally integrated into eleven slices, each spanning an angle of $\sim 32.5^\circ$, giving 11 $S(q)$ scattering curves for every X-ray shot as required to separate the isotropic and anisotropic components of the signal. The azimuthally integrated curves, $S(q)$, were corrected for the non-linear detector response.²⁹ The intensity corrected $S(q)$ were scaled to the theoretical scattering of a liquid unit cell of a 2 mM solution of $\text{Ru}_3(\text{CO})_{12}$ in C_6H_{12} containing one $\text{Ru}_3(\text{CO})_{12}$ surrounded by 4628 C_6H_{12} molecules, in the q -region between 0.7–4.0 \AA^{-1} . The average of the six nearest unpumped patterns was subtracted from each $S(q)$ curve with laser pump to create the difference signals, $\Delta S(q)$. Each $\Delta S(q)$ was time stamped with 10 fs fwhm resolution using the XPP timing tool²⁷ and sorted into time bins each containing ~ 2000 curves. The $\Delta S(q)$ in a given time bin were averaged after outlier rejection based on the in-set median of the $\Delta S(q)$. This resulted in 10–20% of the curves being discarded. This procedure was carried out for each of the eleven $S(q,t)$ producing eleven $\Delta S(q,t)$, which were used to separate the isotropic and anisotropic components of the signal.³⁰ Only the isotropic component of the signal was used for further analysis. In linear combination fitting analysis, the difference scattering curve $q\Delta S(q)$ was further scaled to one solvent molecule, which enables the determination of the excitation fraction of the solute and quantification of the energy release to the solvent. From the point of view of scattering our data are very oversampled (400 points for 11 Shannon channels) with concomitantly high noise. It has been shown, however, that this does not prevent the recovery of accurate scattering curves.³¹

Conclusions

We demonstrated that fs X-ray solution scattering is a robust tool to observe the transient structural kinetics of chemical bond cleavage at the very early stage of a photochemical reaction and possibly reveal optically silent intermediates. Further study with 267 nm excitation of $\text{Ru}_3(\text{CO})_{12}$, which results in the loss of CO, will be interesting to confirm the selective Ru-C bond breakage at higher excitation energies. Possible differences between mechanisms at high and low radiant fluences also remain to be investigated.

Conflicts of interest

There are no conflicts to declare.

Acknowledgements

Use of the Linac Coherent Light Source (LCLS), SLAC National Accelerator Laboratory, is supported by the U.S. Department of Energy, Office of Science, Office of Basic Energy Sciences under Contract No. DE-AC02-76SF00515. KSK gratefully thanks the Danish Council for Independent Research and the Carlsberg Foundation for their support. MMN, EB, and ML gratefully acknowledge support from the Danish Council for Independent Research under grant DFF 4002-00272B, and ML, EB, KH, KSK, MMN gratefully acknowledge DANSCATT for funding the beam time efforts. KJG acknowledges support from the AMOS program within the Chemical Sciences, Geosciences, and Biosciences Division of the Office of Basic Energy Sciences, Office of Science, U. S. Department of Energy. VK and MW gratefully acknowledge support from EU grant Horizon 2020 XPROBE(#637295). The scattering experiment was prepared on ID09 at the ESRF and we would like to acknowledge the support from Denis Leschev.

References

- 1 W. K. Zhang, R. Alonso-Mori, U. Bergmann, C. Bressler, M. Chollet, A. Galler, W. Gawelda, R. G. Hadt, R. W. Hartsock, T. Kroll, K. S. Kjær, K. Kubicek, H. T. Lemke, H. W. Liang, D. A. Meyer, M. M. Nielsen, C. Purser, J. S. Robinson, E. I. Solomon, Z. Sun, D. Sokaras, T. B. Van Driel, G. Vanko, T. C. Weng, D. L. Zhu and K. J. Gaffney, *Nature*, 2014, **509**, 345.
- 2 K. H. Kim, J. G. Kim, S. Nozawa, T. Sato, K. Y. Oang, T. W. Kim, H. Ki, J. Jo, S. Park, C. Song, T. Sato, K. Ogawa, T. Togashi, K. Tono, M. Yabashi, T. Ishikawa, J. Kim, R. Ryoo, J. Kim, H. Ihee and S. Adachi, *Nature*, 2015, **518**, 385.
- 3 T. B. Van Driel, K. S. Kjær, R. W. Hartsock, A. O. Dohn, T. Harlang, M. Chollet, M. Christensen, W. Gawelde, N. E. Henriksen, J. G. Kim, K. Haldrup, K. H. Kim, H. Ihee, J. Kim, H. T. Lemke, Z. Sun, V. Sundstrom, W. K. Zhang, D. L. Zhu, K. B. Moller, M. M. Nielsen and K. J. Gaffney, *Nat. Commun.*, 2016, **7**, 13678.
- 4 S. E. Canton, K. S. Kjær, G. Vanko, T. B. van Driel, S. Adachi, A. Bordage, C. Bressler, P. Chabera, M. Christensen, A. O. Dohn, A. Galler, W. Gawelda, D. Gosztola, K. Haldrup, T. Harlang, Y. Z. Liu, K. B. Moller, Z. Nemeth, S. Nozawa, M. Papai, T. Sato, T. Sato, K. Suarez-Alcantara, T. Togashi, K. Tono, J. Uhlig, D. A. Vithanage, K. Warnmark, M. Yabashi, J. X. Zhang, V. Sundstrom and M. M. Nielsen, *Nat. Commun.*, 2015, **6**, 6359.
- 5 E. Biasin, T. B. van Driel, K. S. Kjær, A. O. Dohn, M. Christensen, T. Harlang, P. Chabera, Y. Z. Liu, J. Uhlig, M. Papai, Z. Németh, R. Hartsock, W. Liang, J. X. Zhang, R. Alonso-Mori, M. Chollet, J. M. Glowonia, S. Nelson, D. Sokaras, T. A. Assefa, A. Britz, A. Galler, W. Gawelda, C. Bressler, K. J. Gaffney, H. T. Lemke, K. B. Møller, M. M. Nielsen, V. Sundström, G. Vankó, K. Wärnmark, S. E. Canton and K. Haldrup, *Phys. Rev. Lett.*, 2016, **117**, 013002.
- 6 H. T. Lemke, K. S. Kjær, R. Hartsock, T. B. van Driel, M. Chollet, J. M. Glowonia, S. Song, D. L. Zhu, E. Pace, S. F. Matar, M. M. Nielsen, M. Benfatto, K. J. Gaffney, E. Collet and M. Cammarata, *Nat. Commun.*, 2017, **8**, 15342.
- 7 M. Levantino, G. Schiro, H. T. Lemke, G. Cottone, J. M. Glowonia, D. L. Zhu, M. Chollet, H. Ihee, A. Cupane and M. Cammarata, *Nat. Commun.*, 2015, **6**, 6772.
- 8 P. Nogly, T. Weinert, D. James, S. Carbajo, D. Ozerov, A. Furrer, D. Gashi, V. Borin, P. Skopintsev, K. Jaeger, K. Nass, P. Båth, R. Bosman, J. Koglin, M. Seaberg, T. Lane, D. Kekilli, S. Brünle, T. Tanaka, W. T. Wu, C. Milne, T. White, A. Barty, U. Weierstall, V. Panneels, E. Nango, S. Iwata, M. Hunter, I. Schapiro, G. Schertler, R. Neutze and J. Standfuss, *Science*, 2018, **361**, 145.
- 9 J. G. Bentsen and M. S. Wrighton, *J. Am. Chem. Soc.*, 1987, **109**, 4530.
- 10 B. F. G. Johnson, J. Lewis and M. V. Twigg, *J. Organomet. Chem.*, 1974, **67**, C75.
- 11 Q. Y. Kong, J. H. Lee, K. H. Kim, J. H. Kim, M. Wulff, H. Ihee and M. H. J. Koch, *J. Am. Chem. Soc.*, 2010, **132**, 2600.
- 12 D. R. Tyler, R. A. Levenson and H. B. Gray, *J. Am. Chem. Soc.*, 1978, **100**, 7888.
- 13 B. Delley, M. C. Manning, D. E. Ellis, J. Berkowitz and W. C. Troglor, *Inorg. Chem.*, 1982, **21**, 2247.
- 14 J. Malito, S. Markiewicz and A. Poe, *Inorg. Chem.*, 1982, **21**, 4335.
- 15 M. F. Desrosiers, D. A. Wink, R. Trautman, A. E. Friedman and P. C. Ford, *J. Am. Chem. Soc.*, 1986, **108**, 1917.
- 16 F. W. Grevels, W. E. Klotzbucher, J. Schrickel and K. Schaffner, *J. Am. Chem. Soc.*, 1994, **116**, 6229.
- 17 E. A. Glascoe, M. F. Kling, J. E. Shanoski and C. B. Harris, *Organometallics*, 2006, **25**, 775.
- 18 T. J. Meyer and J. V. Caspar, *Chem. Rev.*, 1985, **85**, 187.
- 19 X. Q. Dong, F. Yang, J. Zhao and J. P. Wang, *J. Phys. Chem. B*, 2018, **122**, 1296.
- 20 F. W. Vergeer, F. Hartl, P. Matousek, D. J. Stufkens and M. Towrie, *Chem. Commun.*, 2002, 1220.
- 21 Q. Y. Kong, J. H. Lee, H. Plech, M. Wulff, H. Ihee and M. H. J. Koch, *Angew. Chem. Int. Ed.*, 2008, **47**, 5550.
- 22 M. R. Harpham, A. B. Stickrath, X. Y. Zhang, J. Huang, M. W. Mara, L. X. Chen, D. J. Liu, *J. Phys. Chem. A*, **117**, 9807 (2013).
- 23 J. P. Lomont, C. B. Harris, *Inorganica Chimica Acta*, **424**, 38 (2015).
- 24 M. Chollet, R. Alonso-Mori, M. Cammarata, D. Damiani, J. Defever, J. T. Delor, Y. Feng, J. M. Glowonia, J. B. Langton, S. Nelson, K. Ramsey, A. Robert, M. Sikorski, S. Song, D. Stefanescu, V. Srinivasan, D. Zhu, H. T. Lemke and D. M. Fritz, *J. Synchrotron Rad.*, 2015, **22**, 503.
- 25 P. Emma, R. Akre, J. Arthur, R. Bionta, C. Bostedt, J. Bozek, A. Brachmann, P. Bucksbaum, R. Coffee, F. J. Decker, Y. Ding, D. Dowell, S. Edstrom, A. Fisher, S. Gilevich, J. Hastings, G. Hays, Ph. Hering, Z. Huang, R. Iverson, H. Loos, M. Messerschmidt, A. Miahnahri, S. Moeller, H. D. Nuhn, G. Pile, D. Ratner, J. Rzepiela, D. Schultz, T. Smith, P. Stefan, H. Tompkins, J. Turner, J. Welch, W. White, J. Wu, G. Yocky and J. Galayda, *Nat. Photonics*, 2010, **4**, 641.
- 26 K. S. Kjær, T. B. van Driel, J. Kehres, K. Haldrup, D. Khakhulin, K. Bechgaard, M. Cammarata, M. Wulff, T. J. Sorensen and M. M. Nielsen, *Phys. Chem. Chem. Phys.*, 2013, **15**, 15003.
- 27 M. P. Minitti, J. S. Robinson, R. N. Coffee, S. Edstrom, S. Gilevich, J. M. Glowonia, E. Granados, P. Hering, M. C. Hoffmann, A. Miahnahri, D. Milathianaki, W. Polzin, D. Ratner, F. Tavella, S. Vetter, M. Welch, W. E. White and A. R. Fry, *J. Synchrotron Rad.*, 2015, **22**, 526.
- 28 P. A. Hart, A. Dragone, B. Duda, D. Freytag, R. Herbst, S. Herrmann, C. J. Kenney, J. Morse, M. Nordby, J. Pines, G. Haller, S. Boutet, G. Williams, N. van Bakel and G. Carini, *IEEE Nuclear Science Symposium and Medical Imaging Conference (NSS/MIC)*, 2012, 538.
- 29 T. B. van Driel, S. Herrmann, G. Carini, M. M. Nielsen and H. T. Lemke, *J. Synchrotron Rad.*, 2015, **22**, 584.
- 30 U. Lorenz, K. B. Möller and N. E. Henriksen, *New Journal of Physics*, 2010, **12**, 113022.
- 31 P. V. Konarev and D. I. Svergun, *IUCrJ*, 2015, **2**, 352.

Figure captions:

Figure 1. Schematic diagram of ultrafast X-ray solution scattering on the metal-metal bond breakage of $\text{Ru}_3(\text{CO})_{12}$ after 400 nm excitation. **A**, 400 nm excitation of the UV/vis absorption spectrum of $\text{Ru}_3(\text{CO})_{12}$ in cyclohexane corresponds to the metal bonding to antibonding ($4d\sigma \rightarrow 4d\sigma^*$) transition, resulting in Ru-Ru bond cleavage. The green mesh in the inserted molecular orbital of $\text{Ru}_3(\text{CO})_{12}$ represents the metal-metal σ bond. **B**, Femtosecond laser pump and X-ray probe experimental setup at LCLS. The $\text{Ru}_3(\text{CO})_{12}/\text{C}_6\text{H}_{12}$ liquid jet with a thickness of 100 μm is excited by a 30fs laser pulse at 400 nm. A synchronized 40fs X-ray pulse at 9.5 keV arrives after a set time delay and is scattered by the excited solution. The scattered signal is collected by the CSPAD CCD detector. **C**, The X-ray scattering intensity is obtained by azimuthal integration of the 2D scattering pattern. Subtraction of the scattering intensity before laser excitation from that after excitation yields the difference X-ray scattering intensity used to determine the transient molecular structure.

Figure 2. Time-resolved difference X-ray scattering intensities $q\Delta S(q,t)$ at various time delays and structural reaction dynamics of $\text{Ru}_3(\text{CO})_{12}$ in C_6H_{12} 5.16 ps after excitation. **A**, $q\Delta S(q,t)$ (dots) and least-square fits (red lines) between 100 fs and 50 ps. Every 14th delay out of 170 used in the data analysis is presented. The curves are shifted vertically for better visualization. **B**, Contributions to the total theoretical signal (red curve) of the transient solute (blue), solute/solvent interaction (magenta), and response of the bulk solvent due to heat release from hot intermediates (orange). The solute signal is calculated from the Debye scattering of putative solutes, the solute/solvent interaction (cage) from MD simulations, and the solvent signal is deduced from laser heating of a dye molecule in C_6H_{12} excited at 400 nm.²⁶ The strong negative feature at $q = 1.3 \text{ \AA}^{-1}$ and signals below this value arise mainly from solvent heating.²⁶ The positive shoulder at $1.4 < q < 1.8 \text{ \AA}^{-1}$ is a combination of solute and cage with a small contribution from the solvent, while signals at $q > 2 \text{ \AA}^{-1}$ arise mainly from changes in solute structure. Signals at $q > 1.4 \text{ \AA}^{-1}$ can be used as a fingerprint of the transient structure.

Figure 3. Difference X-ray scattering intensities, $q\Delta S(q,t)$. **A**, $q\Delta S(q,t)$ at 100 fs, 5.16 ps and 45 ps. Distinct features are evidence that different transient structures dominate at different time delays. **B**, $q\Delta S(q,t)$ at 100 fs (black) compared with the simulated signal (red) of individual candidate molecular structures used in the linear combination fit. Best agreement between experiment and theory at 100 fs is obtained with $\text{Ru}_3(\text{CO})_{11}(\mu\text{-CO})^*$. **C**, For $q\Delta S(q,t)$ at 5.16 ps (black) compared with the simulated signal (red) the best agreement is obtained with $\text{Ru}_3(\text{CO})_8(\mu\text{-CO})_3^*$. When all intermediates were included in the fit, only $\text{Ru}_3(\text{CO})_{11}(\mu\text{-CO})^*$ and $\text{Ru}_3(\text{CO})_8(\mu\text{-CO})_3^*$ remained at 100 fs and 5.16 ps respectively, while the contribution of other intermediates converged to zero. **D**, The data at 45 ps are consistent with 50 ps data of previous time-resolved X-ray scattering studies where $\text{Ru}_3(\text{CO})_{10}$ was determined to be the major product.²¹ Since both excitations are in the linear region, the difference of the negative feature at $q = 1.3 \text{ \AA}^{-1}$ is most probably due to the use of a pink X-ray beam ($\Delta E/E=3\%$) at ESRF and monochromatic X-ray beam ($\Delta E/E=0.1\%$) at LCLS. Monochromatic X-ray scattering gives a sharp and stronger signal at low q . Broken lines indicate the zero level of each curve in **A**, **B**, **C** and **D**.

Figure 4. Evolution of the population of transient species as a function of time: $\text{Ru}_3(\text{CO})_{11}(\mu\text{-CO})^*$ (black), $\text{Ru}_3(\text{CO})_8(\mu\text{-CO})_3^*$ (blue) and $\text{Ru}_3(\text{CO})_{10}$ (red). Scatter plots are the result of the analysis of individual time delays while the solid curves correspond to global fitting. The dashed and dotted lines represent the time course of the concentrations for reaction rate constants on two sides of the 95% confidence level. The 170 points in the complete data set have been rebinned in groups of three and for clarity only one resulting point in two is shown here with the error bar calculated from the standard deviations of the experimental data. The maximum concentration of $\text{Ru}_3(\text{CO})_{11}(\mu\text{-CO})^*$ (0.52 mM) corresponds to 26% conversion in the photolysis.

Figure 5. Solute-only difference scattering intensities and radial distribution functions. **A**, Solute-only experimental (black) and theoretical (red) difference scattering intensities $q\Delta S(q,t)$ at 100 fs, 5.16ps and 45 ps. **B**, Solute-only difference radial distribution functions $r\Delta S(r,t)$, obtained by Fourier sine transform of **A**. **C**, Selected experimental solute-only difference radial distribution functions $r\Delta S(r,t)$ at different time delays: from top to bottom -1 ps, 100 fs, 95 fs, 760 fs, 1.23 ps, 3.79 ps, 5.16 ps, 6.51 ps, 6.94 ps, 9.87 ps, 41 ps, 45 ps. Broken lines indicate the zero level of each curve in **A**, **B** and **C**.

Figure 6. Reaction pathway of photocleavage of $\text{Ru}_3(\text{CO})_{12}$ in C_6H_{12} following 400 nm excitation. Laser excitation breaks one Ru-Ru bond to form $\text{Ru}_3(\text{CO})_{11}(\mu\text{-CO})^*$, which loses one CO to form $\text{Ru}_3(\text{CO})_8(\mu\text{-CO})_3^*$ at 1.5 ps. The latter loses another CO and yields $\text{Ru}_3(\text{CO})_{10}$ at 10 ps. $\text{Ru}_3(\text{CO})_{10}$ dominates from 10 ps to 100 ns, and rebinds one CO to form $\text{Ru}_3(\text{CO})_{10}(\mu\text{-CO})$ which eventually relaxes to the starting molecule by binding another CO. Ru: cyan, C: gray, O: red.

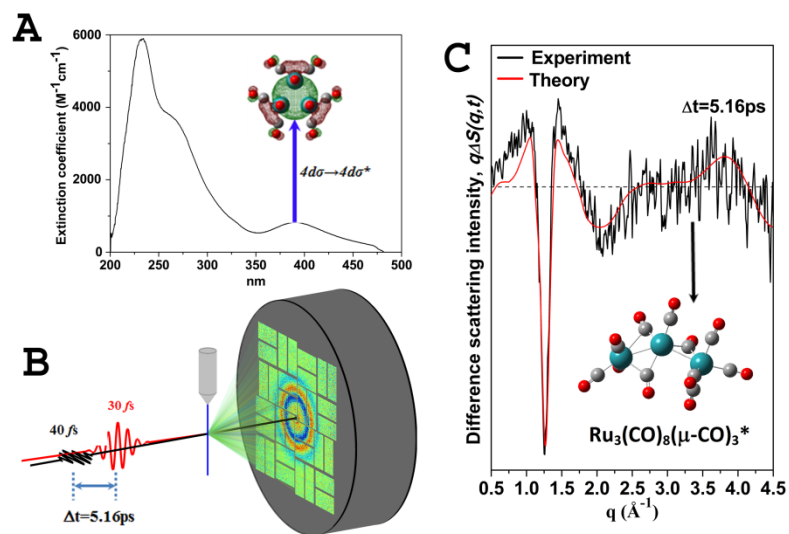


Figure 1

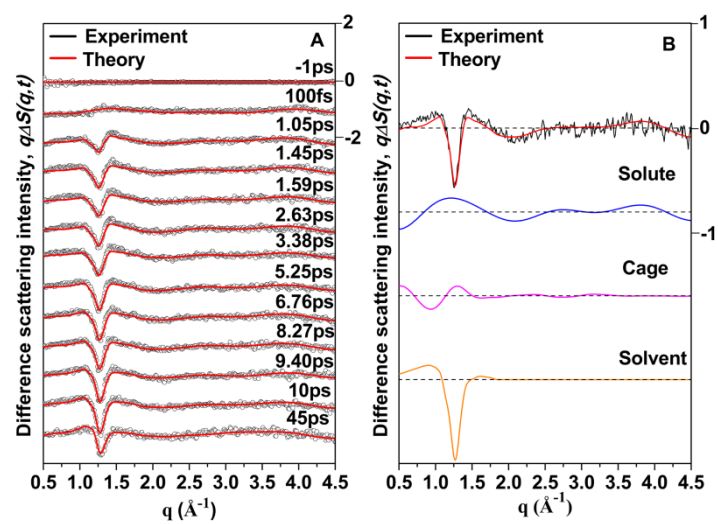


Figure 2

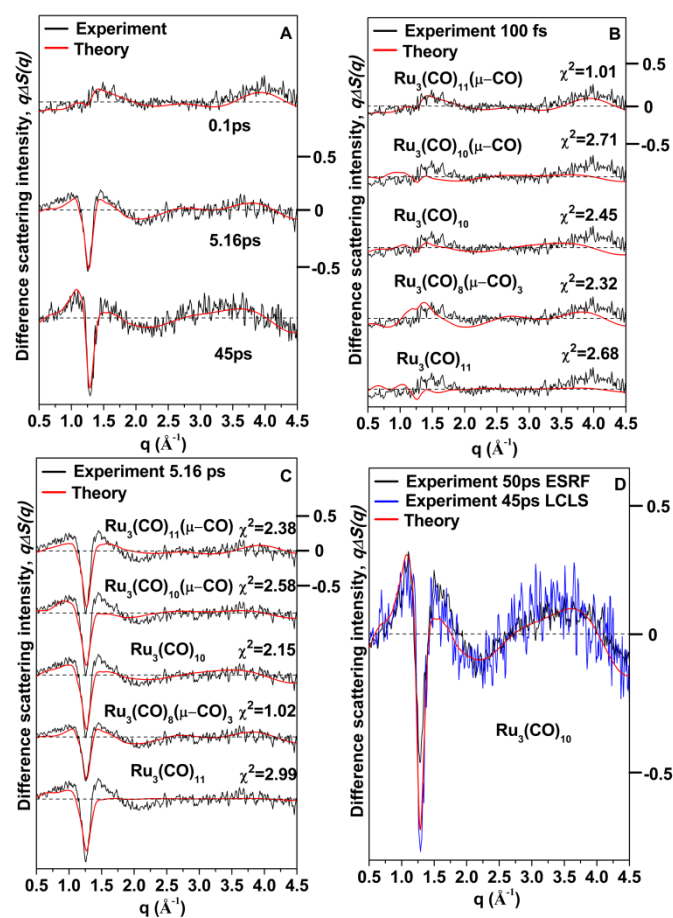


Figure 3

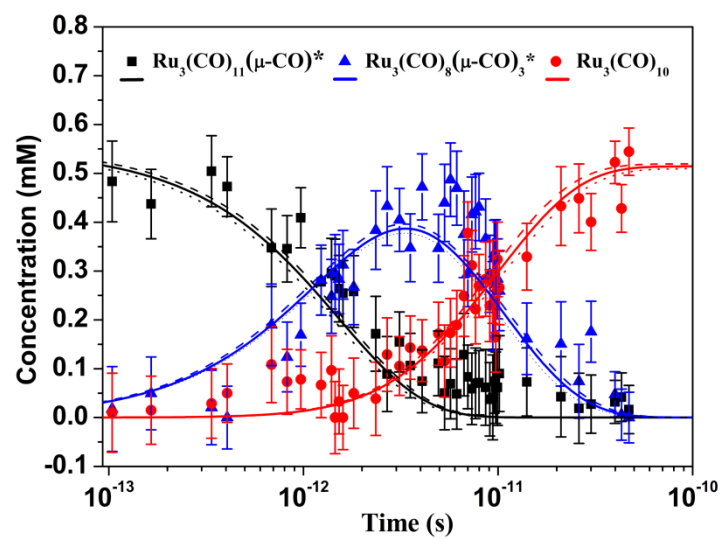


Figure 4

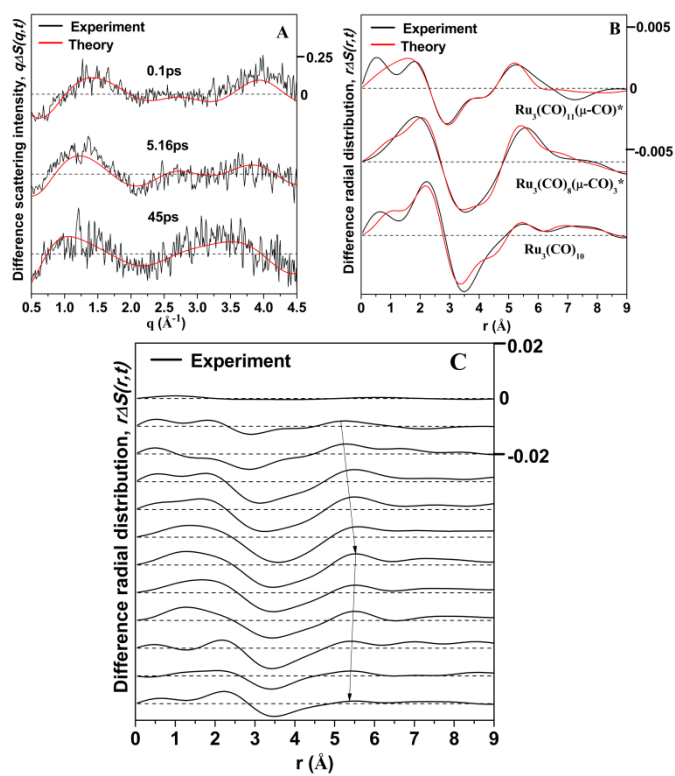


Figure 5

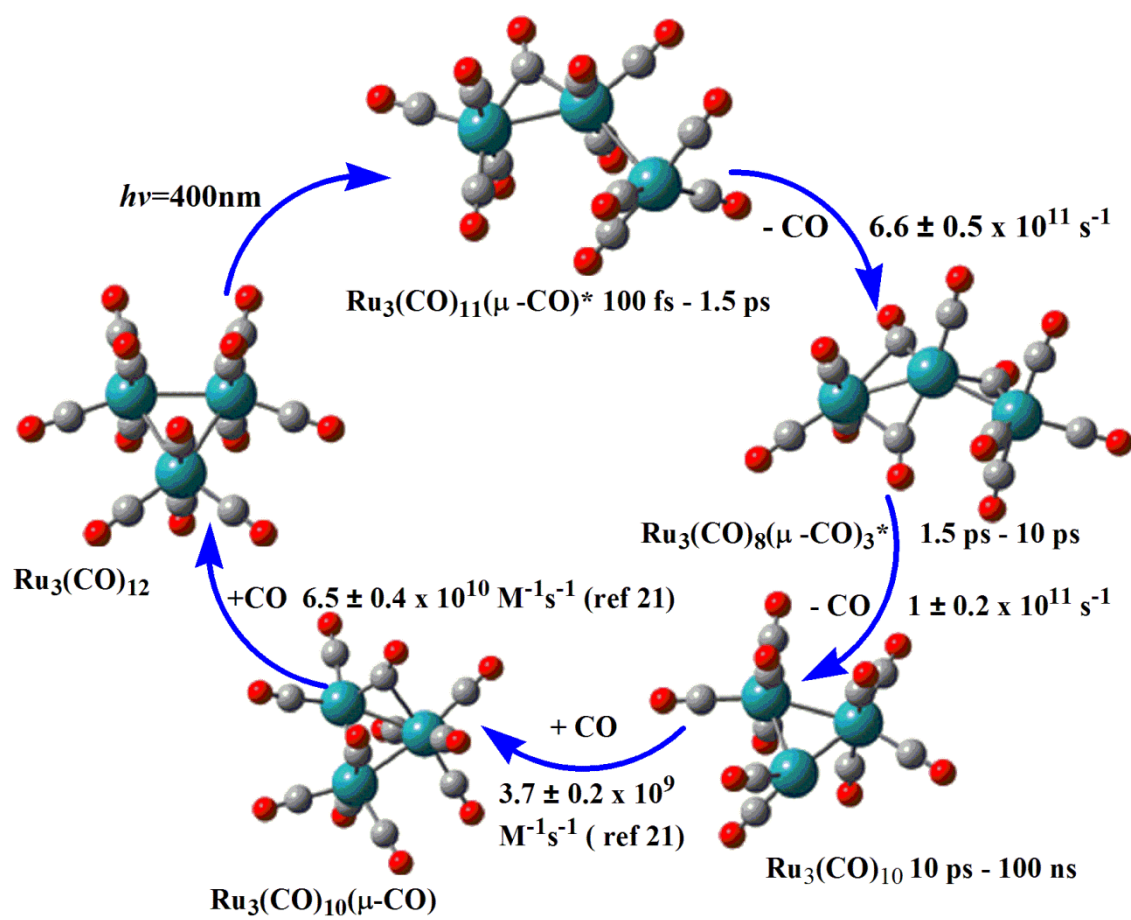


Figure 6